Structural and dynamic inhomogeneities induced by curvature gradients in elliptic colloidal halos of paramagnetic particles

O. A. Ramírez-Garza, J. M. Méndez-Alcaraz, and P. González-Mozuelos

Citation: The Journal of Chemical Physics **146**, 194903 (2017); doi: 10.1063/1.4983496
View online: http://dx.doi.org/10.1063/1.4983496
View Table of Contents: http://aip.scitation.org/toc/jcp/146/19
Published by the American Institute of Physics

Structural and dynamic inhomogeneities induced by curvature gradients in elliptic colloidal halos of paramagnetic particles

O. A. Ramírez-Garza,[a] J. M. Méndez-Alcaraz,[b] and P. González-Mozuelos[c]
Departamento de Física, Cinvestav del I. P. N., Ave. Instituto Politécnico Nacional 2508, Col. San Pedro Zacatenco, Ciudad de México, C.P. 07360, Mexico

(Received 23 January 2017; accepted 3 May 2017; published online 16 May 2017)

Paramagnetic colloidal particles distributed along an ellipse are used as a model system to study the effects of curvature gradients on the structure and dynamics of colloids in curved manifolds. Unlike what happens for circular and spherical systems, in the present case, the equilibrium one-particle distribution function displays inhomogeneities due to the changing curvature along the ellipse. The ensuing effects on the two-body correlations are also analyzed, leading to the observation of anisotropic and long-ranged effects. Another noticeable consequence is the slowing down of the self-diffusion of these particles, which for large eccentricities may induce metastable states; this is evaluated by means of the time-dependent self-distribution. *Published by AIP Publishing.* [http://dx.doi.org/10.1063/1.4983496]

I. INTRODUCTION

The properties of colloids in curved manifolds are important in biophysics, colloidal science, and nanotechnology, among other fields, due to their close relation to important phenomena and technological challenges, as it is the case for the diffusion of proteins on membranes,[1–3] the diffusion of particles along narrow channels,[4] the controlled synthesis of nanometric colloidal aggregates,[5,6] etc. In this paper, we explore the effects of curvature gradients on those properties by using elliptic distributions of paramagnetic particles as model systems—these being simple enough, yet clearly illustrative of the main issues of interest. For this purpose, we implement on our elliptic systems the extension to curved manifolds, first developed by Castro Villarreal and collaborators,[7] of the Ermak-McCammon Brownian Dynamics (BD) algorithm,[8] which is part of several recent theoretical, computer simulation, and experimental contributions that have greatly advanced our understanding of diffusion and structure in curved varieties.[9–13] This approach has been previously applied to colloidal particles confined to circles and spheres,[7,14] thus allowing us to compare the present results against those in which the curvature is constant. In the particular case of circles, where this has been done for paramagnetic particles too, the mean-square angular displacement has been used to study their dynamics. The main finding was the existence of a sub-diffusive regime at intermediate times, due to the fact that the particles cannot pass each other when confined to these one-dimensional manifolds.[4,7,14–16] The static structure, on the other hand, has been investigated by means of the two-particle angular distribution function.[17]

Paramagnetic particles are considered in our theoretical models because they allow for the synthesis of very interesting experimental realizations of the two-dimensional colloidal arrays,[4,18] thus making them viable potential candidates for an experimental implementation of our one-dimensional elliptic systems. This could be done, in principle, by using channels fabricated with photolithography[4] or through scanning optical tweezers confining the particles[16] or by allowing them to get adsorbed onto a neutral elliptic substrate in order to build elliptic halos.[17,19] This last instance is the reason why we denote halos these kind of systems.

Elliptic halos are expected to behave differently from the circular ones due to the changing curvature along the perimeter. The structure, for instance, is expected to become inhomogeneous. Therefore, the diffusion of the particles along the ellipses should be similar to the case of diffusing particles in ragged energy landscapes,[20] but with the degree of difficulty increased by the fact that our systems are one-dimensional, curved (with curvature gradients), finite, confined, closed, and periodic. To face this situation, we have to give up the mean-square angular displacement as the suitable dynamic parameter and consider instead the whole time-dependent one-particle distribution function from the beginning; the structure, in turn, is investigated by means of the inhomogeneous two-particle angular distribution function. The present study thus reports the consequences of varying the eccentricity of the ellipse, the strength of the interactions among the confined particles, and the one-dimensional density of such particles.

The details of the computer simulations and calculated quantities are explained, after this brief introduction, in Section II. The model system is then presented in Section III, while the corresponding results are discussed in Section IV. The paper ends with some concluding remarks in Section V.

II. COMPUTER SIMULATIONS

The approach considered here is based on the extension to curved manifolds of the Ermak-McCammon[8] Brownian Dynamics (BD) algorithm developed by Castro Villarreal *et al.*[7] Here, we are interested in the behavior of a system of N identical particles constrained to move on a

[a]Electronic mail: oaramirez@fis.cinvestav.mx
[b]Electronic mail: jmendez@fis.cinvestav.mx
[c]Electronic mail: pedro@fis.cinvestav.mx

curve described by the parametric expression

$$\mathbf{X}(\alpha) = x(\alpha)\,\hat{x} + y(\alpha)\,\hat{y} + z(\alpha)\,\hat{z}\,, \tag{1}$$

where $\alpha_0 \leq \alpha \leq \alpha_f$, so the distance along the curve associated to the value α is given by

$$s(\alpha) = \int_{\alpha_0}^{\alpha} d\gamma \left(\frac{d\mathbf{X}(\gamma)}{d\gamma} \cdot \frac{d\mathbf{X}(\gamma)}{d\gamma} \right)^{1/2}, \tag{2}$$

whereas

$$\mathbf{T}(\alpha) = \left(\frac{d\mathbf{X}(\alpha)}{d\alpha} \cdot \frac{d\mathbf{X}(\alpha)}{d\alpha} \right)^{-1/2} \frac{d\mathbf{X}(\alpha)}{d\alpha} \tag{3}$$

is the corresponding unit tangent vector. It is also assumed here that this curve is simple (it does not self-intersect), smooth (the unit tangent vector is continuous), and closed ($\mathbf{X}(\alpha_0) = \mathbf{X}(\alpha_f)$ with $\mathbf{T}(\alpha_0) = \mathbf{T}(\alpha_f)$). Hence, the particular microstate of this system at time t is determined by the location of each particle along this one-dimensional space, that is, by the set of values $\{\alpha_1(t), \ldots, \alpha_N(t)\}$; alternatively, we can use the set of arc lengths $\{s_1(t), \ldots, s_N(t)\}$ to describe such a microstate.

For this one-dimensional system, the BD algorithm[7] prescribes a displacement in the position of the m-particle when going from t to $t + \delta t$ given by

$$s_m(t + \delta t) = s_m(t) + \frac{D_0}{k_B\,T}\,\mathcal{F}_m(t)\,\delta t + \mathcal{R}_m(\delta t)\,, \tag{4}$$

where D_0 is the free-particle diffusion coefficient, k_B is the Boltzmann constant, T is the temperature of the system, $\mathcal{F}_m(t)$ is the tangent component of the deterministic force acting on the m-particle at time t, and $\mathcal{R}_m(\delta t)$ is a Gaussian distributed random number such that

$$\langle \mathcal{R}_m(\delta t) \rangle = 0 \quad \text{and} \quad \left\langle \left(\mathcal{R}_m(\delta t) \right)^2 \right\rangle = 2\,D_0\,\delta t\,, \tag{5}$$

where $\mathcal{R}_m(\delta t)$ represents the movement induced by the tangent stochastic force due to the collisions of the solvent molecules with the m-particle. For our periodic systems, the displacement prescribed in (4) may take the particle beyond its boundaries, in which case the transformations $s_m(t+\delta t) \to s_m(t+\delta t) - P$ when $s_m(t+\delta t) > P$ and $s_m(t+\delta t) \to s_m(t+\delta t) + P$ when $s_m(t+\delta t) < 0$ are applied, where P is defined below. For a colloidal particle of diameter σ, the free-diffusion coefficient is usually given by the Stokes-Einstein formula $D_0 = k_B\,T/(3\pi\,\eta\,\sigma)$, where η is the viscosity of the solvent. Let $P = s(\alpha_f)$ be the perimeter (total arc length) of the curve, then δt should be small enough to ensure that $|s_m(t + \delta t) - s_m(t)| << P/N$, and in fact the derivation of (4) requires that δt is small enough to guarantee that the deterministic force $\mathcal{F}_m(t)$ remains basically constant during the corresponding displacement (at short-times the particles thus diffuse freely). Nonetheless, the derivation of (4) is also contingent on considering the limit $\delta t >> M/(3\pi\,\eta\,\sigma)$, where M is the mass of each particle, to ensure that we are indeed working within the Smoluchowski regime of the dynamics.[21]

Neglecting the hydrodynamic interactions and any external field, we find that the deterministic tangent force is determined by

$$\mathcal{F}_m(t) = \sum_{n=1}^{N} \mathbf{T}(\alpha_m(t)) \cdot \mathbf{F}_{mn}(t)\,, \tag{6}$$

where

$$\mathbf{F}_{mn}(t) = f\left(|\mathbf{X}(\alpha_m(t)) - \mathbf{X}(\alpha_n(t))|\right) \times \frac{\mathbf{X}(\alpha_m(t)) - \mathbf{X}(\alpha_n(t))}{|\mathbf{X}(\alpha_m(t)) - \mathbf{X}(\alpha_n(t))|}, \tag{7}$$

for $m \neq n$, is the force exerted by the n-particle on the m-particle at time t, while the self-force is null, that is, $\boldsymbol{F}_{mm}(t) = 0$. This last expression fulfills, indeed, Newton's third law. Given the pair-wise interaction potential between any two particles $u(r)$, then

$$f(r) \equiv -\frac{du(r)}{dr} \tag{8}$$

determines the magnitude of these forces (the sign on the right side of Equation (8) is determined by our choice of the unit vector in Equation (7)). The contribution from the stochastic force, on the other hand, can also be described as the tangent component of the vector force exerted by the solvent on the m-particle, so

$$\mathcal{R}_m(\delta t) = \mathbf{T}(\alpha_m(t)) \cdot \mathbf{R}_m(\delta t), \tag{9}$$

where each Cartesian component, $\hat{x} \cdot \mathbf{R}_m(\delta t)$, $\hat{y} \cdot \mathbf{R}_m(\delta t)$, and $\hat{z} \cdot \mathbf{R}_m(\delta t)$, is again Gaussian distributed with the same properties given in (5); of course, the net result behaves as detailed above.

Let $\rho(s)$ be the equilibrium one-particle distribution, that is, $\rho(s)\,ds$ is the average number of particles within the interval between s and $s + ds$. For a system of non-interacting particles, where all the deterministic forces are null, the relationship (4) indicates that the displacement of each particle becomes independent of its position along the curve, and consequently $\rho(s)$ becomes independent of s too; that is, in this case, we have $\rho(s) = N/P$. It is then convenient to introduce the one-body distribution function

$$g_w(s) \equiv \frac{P}{N}\,\rho(s) \tag{10}$$

as a first measure of the static microstructure of this kind of system. Therefore, $g_w(s) = 1$ not only for a system of non-interacting particles but also for a system of interacting particles confined to move along a circle, which is characterized by its globally uniform and isotropic geometry. The deviations of $g_w(s)$ from unity hence provide, in the absence of an external field, information about the global shape of the curve $\mathbf{X}(\alpha)$.

Further information about the static microstructure is obtained from the two-body correlations described by the conditional density $\rho(s_0; s)$, where $\rho(s_0; s)\,ds$ is the average number of particles within the interval between s and $s + ds$ given that there is a particle fixed at the position s_0. Here, it is also convenient to introduce the normalized, dimensionless distribution function[22]

$$g(s_0, s) \equiv \frac{\rho(s_0; s)}{\rho(s)} \tag{11}$$

to account for the particle-particle correlations. Thus, for a uniform and isotropic system, again in the absence of an external field, we get that $g(s_0, s) = g(|s_0 - s|)$; this is the distribution function discussed in previous studies.[17,23] And once more, $g(s_0, s) = 1$ for a system of non-interacting particles, regardless of the shape of $\mathbf{X}(\alpha)$.

With respect to the dynamic properties of these one-dimensional systems, it is useful to consider the tagged-particle self-distribution function

$$\rho^{(s)}(s_0; s, t) = \langle \delta(s - s_1(t)) \rangle \,, \tag{12}$$

where the labeled particle is the 1-particle and $s_0 = s_1(0)$ is its initial position. Therefore, $\rho^{(s)}(s_0; s, t)\, ds$ is the probability of finding the tagged particle in the interval between s and $s + ds$ at time t; of course, we have $\rho^{(s)}(s_0; s, 0) = \delta(s - s_0)$. For a system of non-interacting particles, we also get $\lim_{t\to\infty} \rho^{(s)}(s_0; s, t) = 1/P$, and this result is still valid for interacting particles when they are confined to a planar circle in the absence of an external field.

For the case of circles, as it is shown in Section IV, we have that $\rho^{(s)}(s_0; s, t)$ looks like a symmetric Gaussian bell centered on s_0 that broadens as t increases. For a system of interacting particles confined to an arbitrary curve $\mathbf{X}(\alpha)$, on the other hand, the shape of $\rho^{(s)}(s_0; s, t)$ becomes more complex, as it portrays the intricate interplay between the inter-particle interactions and the global geometry. Yet the asymptotic time limit of the self-distribution function is, in this general case, given by the equilibrium probability density, that is,

$$\lim_{t\to\infty} \rho^{(s)}(s_0; s, t) = \frac{\rho(s)}{N} \,, \tag{13}$$

and consequently the long-term self-distribution becomes independent of the initial position of the tagged particle.

III. MODEL SYSTEM

To illustrate the issues discussed above let us consider here a system of colloidal particles confined to a simple elliptic path lying on the $z = 0$ plane,

$$\mathbf{X}(\alpha) = a\, \cos\alpha\, \hat{x} + b\, \sin\alpha\, \hat{y} \,, \tag{14}$$

where a is the length of the semi-major axis and b is the length of the semi-minor axis, so $a \geq b$ and $\varepsilon \equiv \sqrt{1 - b^2/a^2}$ is the related eccentricity. The corresponding arc length and unit tangent vector are given by

$$s(\alpha) = a \int_0^\alpha d\gamma \sqrt{1 - \varepsilon^2 \cos^2\gamma} \tag{15}$$

and

$$\mathbf{T}(\alpha) = \frac{-a\, \sin\alpha\, \hat{x} + b\, \cos\alpha\, \hat{y}}{a\,(1 - \varepsilon^2 \cos^2\alpha)^{1/2}} \,, \tag{16}$$

respectively. Thus, for $\varepsilon = 0$ we recover the uniform isotropic case used here as the benchmark: a circle with radius $b = a$.

We shall also assume that the colloids enclosed within this elliptic path are identical paramagnetic particles subject to the action of a uniform and constant external magnetic field $\mathbf{H}$ perpendicular to the plane of the ellipse, that is, $\mathbf{H} = H\,\hat{z}$. This external field induces parallel magnetic dipoles of magnitude $M = \xi_{eff}\, H$ within each colloid, where ξ_{eff} is the corresponding effective magnetic susceptibility, so outside the hard-core repulsion, the interaction potential is given by $u(r) = \mu_0\, M^2/(4\pi\, r^3)$. Of course, for $r < \sigma$, the hard-sphere potential comes into play, yet for large enough magnetic fields the dipole-dipole repulsion becomes sufficiently strong to prevent the colloids from touching, so we shall assume here that the r^{-3} form of the potential prevails for all separation distances. Consequently, the force magnitude appearing in (7) is given by

$$f(r) = 3\, k_B\, T\, \frac{\Gamma}{\sigma} \left(\frac{\sigma}{r}\right)^4 , \tag{17}$$

where $\Gamma \equiv \mu_0\, \xi_{eff}^2\, H^2/(4\pi\, k_B\, T\, \sigma^3)$ is the dimensionless strength parameter of the pair potential.[18] The value $\Gamma = 125$ taken for most of our calculations (see Section IV) roughly corresponds to the value 8.2 in the parameter scales used by Zahn *et al.*[18]

Since the positions $\mathbf{X}(\alpha_m(t))$ are needed at all times to calculate the forces among the particles, and consequently the set of values $\{\alpha_1(t), \ldots, \alpha_N(t)\}$ is required at each step, the particular implementation of the algorithm considered here, taking into account (4) and (15) with the mean value theorem, assumes the form

$$\alpha_m(t + \delta t) = \alpha_m(t) + \frac{\sigma}{a}\, \frac{\mathcal{F}_m^*(t)\,(\delta t/\tau_0) + \mathcal{R}_m^*(\delta t)}{(1 - \varepsilon^2 \cos^2\alpha_p)^{1/2}} \,, \tag{18}$$

where $\mathcal{F}_m^*(t) \equiv \sigma\, \mathcal{F}_m(t)/(k_B\, T)$ and $\mathcal{R}_m^*(\delta t) \equiv \mathcal{R}_m(\delta t)/\sigma$ are the dimensionless deterministic force and random jump, respectively, whereas $\tau_0 \equiv \sigma^2/D_0$ is the time that a free particle takes to diffuse a distance equivalent to its own diameter. Moreover, $f^*(r) \equiv \sigma f(r)/(k_B\, T) = 3\,\Gamma\,(\sigma/r)^4$ is the related dimensionless force magnitude, while $\mathcal{R}_m^*(\delta t)$ has, indeed, a null mean value and variance $2\,(\delta t/\tau_0)$. This still leaves open the specific value assumed for α_p, which may be any value in the closed interval between $\alpha_m(t)$ and $\alpha_m(t + \delta t)$.

The simplest choice is of course $\alpha_p = \alpha_m(t)$, but this has the shortcoming of overestimating (underestimating) the displacements away (toward) the vertices of maximum curvature. Thus, a predictor-corrector approach needs to be implemented within this algorithm: first, we determine the initial guess $\alpha_m^{(0)}(t + \delta t)$ taking $\alpha_p = \alpha_m(t)$; afterwards successive values $\alpha_m^{(n)}(t + \delta t)$ are determined using $\alpha_p = (\alpha_m^{(n-1)}(t + \delta t) + \alpha_m(t))/2$. We tested this approach by using the benchmark $g_w(s) = 1$ for different eccentricities in the case of $\Gamma = 0$ and found that two iterations ($n = 2$) worked fine for $\varepsilon \leq 0.99$; hence $\alpha_m(t + \delta t) = \alpha_m^{(2)}(t + \delta t)$ is recorded and used for the next simulation step. Also, the transformations $\alpha_m(t + \delta t) \to \alpha_m(t + \delta t) - 2\pi$ when $\alpha_m(t + \delta t) > 2\pi$ and $\alpha_m(t + \delta t) \to \alpha_m(t + \delta t) + 2\pi$ when $\alpha_m(t + \delta t) < 0$ are applied after such a step.

The BD time step $\delta t = 0.0001\, \tau_0$, corresponding to displacements with average magnitude roughly of the order of $0.014\, \sigma$, was used here to ensure that the forces remain basically constant during each basic BD jump. At first, the particles were set at the positions $\alpha_m = \alpha_0 + 2(m - 1)\pi/N$ for $m = 1, \ldots, N$, so α_0 is the initial position of the 1-particle, and subsequently 5×10^6 time steps were used to thermalize the system in all cases. Once the thermalization process was finished, the resulting positions were set as the initial set $\{\alpha_1(0), \ldots, \alpha_N(0)\}$ for the proper time evolution of the equilibrium system, for which 40×10^6 time steps were taken in all cases; the final time is thus $t_{max} = 4000\, \tau_0$. The angle coordinates $\{\alpha_1(t), \ldots, \alpha_N(t)\}$ were then transformed, when needed, into the arc length coordinates $\{s_1(t), \ldots, s_N(t)\}$ using the relationship (15), which is evaluated numerically as a table. To facilitate comparisons among systems with different eccentricities, the total arc length of the ellipse was kept fixed to the

value $P = 60\,\sigma$, and consequently the value of a varies as a function of ε (additionally, t_{max} is thus enough for a free particle to diffuse almost 70 times around the ellipse). If we take, for instance, the experimental parameters used by Zahn and collaborators,[18] then $\delta t \approx 0.02$ s and $t_{max} \approx 11$ days. The last is not an infinite time, but close enough for an ordinary colloidal particle—and beyond the current experimental possibilities of recording its motion without any interruption.[4,16,24]

To analyze and characterize the static and dynamic properties of this kind of systems, three types of simulation runs were considered in the present study for each value set of the system parameters N, ε, and Γ. In the first instance, used to determine the one-body distribution function $g_w(x)$, all the particles are allowed to move according to the algorithm prescribed in Equation (18) during both the thermalization process and the proper time evolution of the system. In order to evaluate the two-body distribution functions $g(s_0, s)$, on the other hand, the 1-particle position $\alpha_1(t)$ was kept fixed during both stages, so $\alpha_1(t) = \alpha_0$ at all times, while the remaining particles were displaced according to (18). In these two types of simulation runs, the particle coordinates were sampled each 5000 BD time steps during the proper evolution stage, to lessen the effects of time correlations, and the 8000 stored configurations were employed to perform time averages of the occupation numbers in each slot of a uniform arc length grid with intervals of width $0.1\,\sigma$. Additionally, the resulting histograms were also averaged over 6400 tries with different seeds for the random number generator to obtain, after suitable normalization, the results for $g_w(x)$ and $g(s_0, s)$ presented here. That is, we are averaging over an ensemble of 6400 identical copies of each system. A discussed below, this last procedure avoids the system getting stuck into metastable states.

For the third type of simulation run, devised to ascertain the self-distribution function $\rho^{(s)}(s_0; s, t)$, the position of the 1-particle, the tagged particle, was kept fixed only during the thermalization phase of the simulation, while the remaining particles were indeed evolved in accord to (18) during this period. Subsequently, the tagged particle was released for the corresponding proper time evolution, so the whole set $\{\alpha_1(t), \ldots, \alpha_N(t)\}$ was progressed at this stage by the algorithm stipulated in (18). In this approach, $\alpha_1(0)$ is thus a specified parameter, $\alpha_1(0) = \alpha_0$, and the task is settled by tracking $\alpha_1(t)$ at established values of t. Of course, $s_0 = s(\alpha_0)$. In this instance, the number of times that the tagged particle fell at time t into a given slot of an arc length grid, now with intervals of width $0.8\,\sigma$, was averaged over 51 200 tries with different seeds for the random number generator (that is, the average is taken over an ensemble of 51 200 identical copies of each system). The ensuing histograms, properly renormalized, thus yield the reported functions $\rho^{(s)}(s_0; s, t)$.

IV. RESULTS

Figure 1 illustrates the one-body distribution functions $g_w(s)$ corresponding to $\Gamma = 125$ and three particle numbers ($N = 8$, 9, and 10) for the following eccentricity values: $\varepsilon = 0.98$ (thus $a = 14.284\,\sigma$ and $b = 2.843\,\sigma$) in panel (a) and $\varepsilon = 0.99$ (thus $a = 14.585\,\sigma$ and $b = 2.057\,\sigma$) in panel (b). As explained

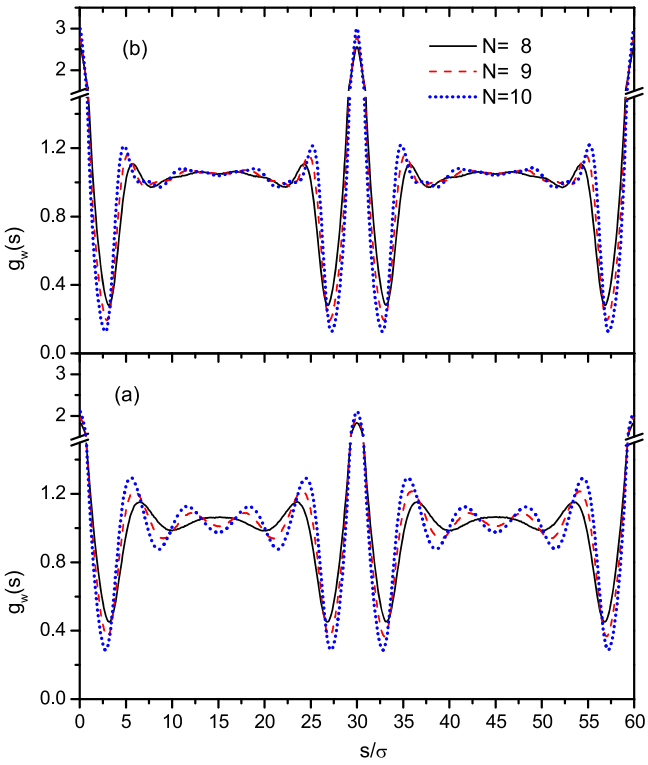

FIG. 1. The one-body distribution functions $g_w(s) \equiv \rho(s)P/N$ corresponding to $\Gamma = 125$ and the following eccentricity values: $\varepsilon = 0.98$ in panel (a) and $\varepsilon = 0.99$ in panel (b).

above, $g_w(s) = 1$ for $\varepsilon = 0$ (in which case $a = b = 9.549\,\sigma$). In all cases, there are two very noticeable peaks centered at $s/\sigma = 0$ (= 60) and $s/\sigma = 30$, respectively, indicating the system's preference for having one particle trapped at each one of these extreme vertices, where the curvature is largest. This is certainly due to the long-ranged repulsions among the confined particles, since the trend clearly increases as the particle linear density grows. This effect is amplified too as the eccentricity becomes larger.

A perhaps more interesting effect in this instance is the accompanying loss of structure: for example, for $N = 10$, the four peaks in the region between $s \approx 2.5\,\sigma$ and $s \approx 27.5\,\sigma$ (or those between $s \approx 32.5\,\sigma$ and $s \approx 57.5\,\sigma$) are certainly more evident for $\varepsilon = 0.98$ than for $\varepsilon = 0.99$. These peaks suggest, for this case, the presence of four particles in the upper (lower) region of the ellipse, and the reason for they being less marked for the more elongated loop is surprisingly due to the reduced particle diffusion between its superior and inferior halves, which is in turn brought about by the near immobility of the particles at the extremes. This explanation is contradictory only in appearance, since the structure for the $N = 10$ and $\varepsilon = 0.99$ case is in fact the average of many instances in which 3, 4, or 5 particles are practically confined to the upper (lower) half of the ellipse. The equilibrium distribution then emerges from the weighted sum of these metastable states, and this clearly demonstrates the advantage of averaging over a large number of seeds for the random number generator.

The results for the two-body distribution function $g(s_0, s)$ corresponding to the values $N = 10$ and $\Gamma = 125$ are presented in Figures 2 and 3. The large narrow peak located at s_0 in all these plots pinpoints the location of the fixed

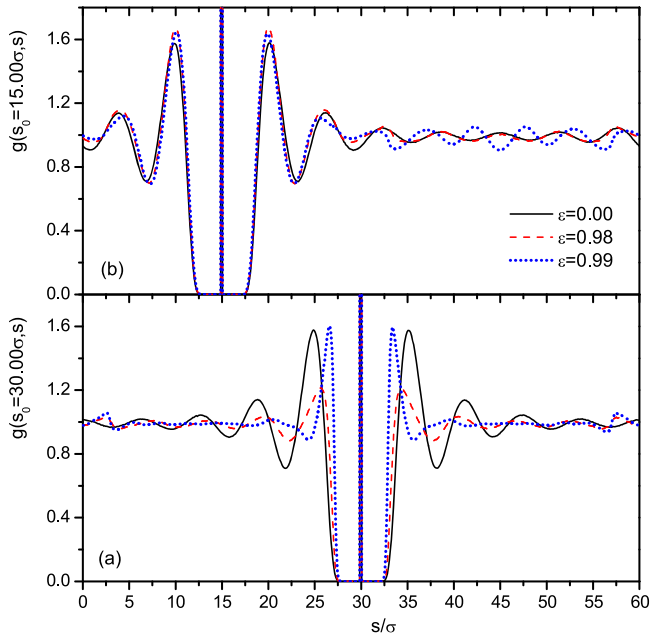

FIG. 2. The two-body distribution functions $g(s_0, s)$ corresponding to $N = 10$ and $\Gamma = 125$ for the reference positions: $s_0 = 30.00\,\sigma$ in panel (a) and $s_0 = 15.00\,\sigma$ in panel (b).

particle and thus represents the self-correlation component of $g(s_0, s)$. The cases of $s_0 = 15.00\,\sigma$ and $s_0 = 30.00\,\sigma$ are shown in the top and bottom panels, respectively, of Figure 2. These distributions are symmetric under reflections with respect to the axis on which the fixed particle is sitting: the y-axis in the first case and the x-axis in the second. As commented above, those belonging to $\varepsilon = 0$ have, in addition, the property $g(s_0, s) = g(|s - s_0|)$, that is, the pertinent plot in panel (a) is identical to the corresponding one in panel (b) after being accordingly shifted. Hence, the comparison of these plots against those illustrating the cases with $\varepsilon = 0.98$ and $\varepsilon = 0.99$ showcase the

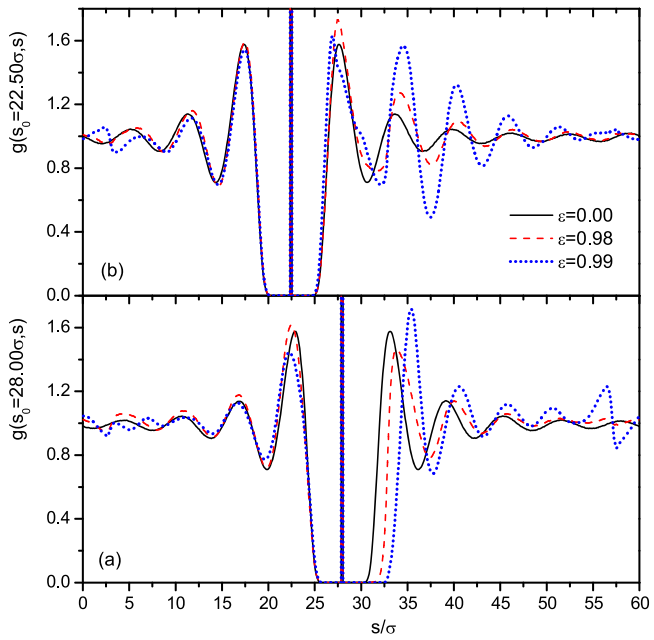

FIG. 3. The two-body distribution functions $g(s_0, s)$ corresponding to $N = 10$ and $\Gamma = 125$ for the reference positions: $s_0 = 28.00\,\sigma$ in panel (a) and $s_0 = 22.50\,\sigma$ in panel (b).

impact of the non-uniform curvature on the particle-particle correlations.

For $s_0 = 15.00\,\sigma$, the peaks of $g(s_0, s)$ in the vicinity of s_0 are rather similar for the three values of ε, albeit not identical, yet beyond this region the structure of these distribution functions becomes clearly more divergent. For $s_0 = 30.00\,\sigma$, on the other hand, the peaks of $g(s_0, s)$ in the vicinity of s_0 are more diverse, with their position moving inward as ε increases, though the corresponding height does not vary monotonically, since it first decreases and afterwards rises. Further away from the fixed particle, the structure of $g(s_0, s)$ seems, for this case, to be less marked for the elongated loops than for the circle, yet near the opposite vertex there is a small but distinct boosting of the oscillations.

The distance at which $\beta u(r) \approx 1$, roughly the separation of the first peaks of $g(s_0, s)$ from the fixed particle, can be considered as the effective hard-sphere diameter of the colloidal particles. It is of the order of $\Gamma^{1/3}$ (approximately 5σ for the present situation), and thus larger than the length $2b$ for the case of $\varepsilon = 0.99$; therefore, for this instance, the particles on the upper side of the loop are basically touching those on the lower side. However, the expected exclusions are not displayed in Figs. 2 and 3, since the symmetry around s_0 is restored after averaging over the 6400 identical copies of each system.

Two less symmetric situations are portrayed in Figure 3, where the cases of $s_0 = 28.00\,\sigma$ and $s_0 = 22.50\,\sigma$ are shown in panels (a) and (b), respectively. In the upper panel, the fixed particle is thus at the middle point between the top and left vertices, and the shape of $g(s_0, s)$ for the three eccentricity cases looks quite similar when moving clockwise (into the straightest part of the ellipses), while in the opposite direction there is clearly more discrepancy. It is also noteworthy to observe that the most elongated system appears to have more structured correlations in the region $30\,\sigma < s < 60\,\sigma$ than the other two cases, due to the interference between the upper and lower halves of the loop. In the instance presented in the lower panel, the fixed particle is just $2.0\,\sigma$ counterclockwise from the extreme left vertex, thus pushing off any particle that may have been sitting there. The ensuing shape of $g(s_0, s)$ for $s > 30\,\sigma$ indicates that the corresponding first neighbor moves further away, while the accompanying oscillations become more structured, as the eccentricity rises. Going in the opposite direction there is also a departure from the case of uniform curvature when ε increases, though this seems rather less marked by comparison.

The behavior of the time-dependent self-distribution function $\rho^{(s)}(s_0; s, t)$ for $N = 10$ and $\Gamma = 125$ is depicted in Figures 4 and 5, corresponding to $s_0 = 30.00\,\sigma$ and $s_0 = 22.50\,\sigma$, respectively, where three eccentricities are reported: $\varepsilon = 0$ in panel (a), $\varepsilon = 0.98$ in panel (b), and $\varepsilon = 0.99$ in panel (c). Therefore, at the bottom of both figures we have the system with uniform curvature, and as expected, in this instance, the results corresponding to $s_0 = 22.50\,\sigma$ are identical, within the error bars, to those corresponding to $s_0 = 30.00\,\sigma$ after the proper displacement. We can observe too that for the longest time reported, $t = 4000\,\tau_0$, the self-distribution function has already reached the equilibrium uniform distribution $\lim_{t\to\infty} \rho^{(s)}(s_0; s, t) = 1/P$ associated to the $\varepsilon = 0$ case, whereas at times $t = 15\,\tau_0$ and

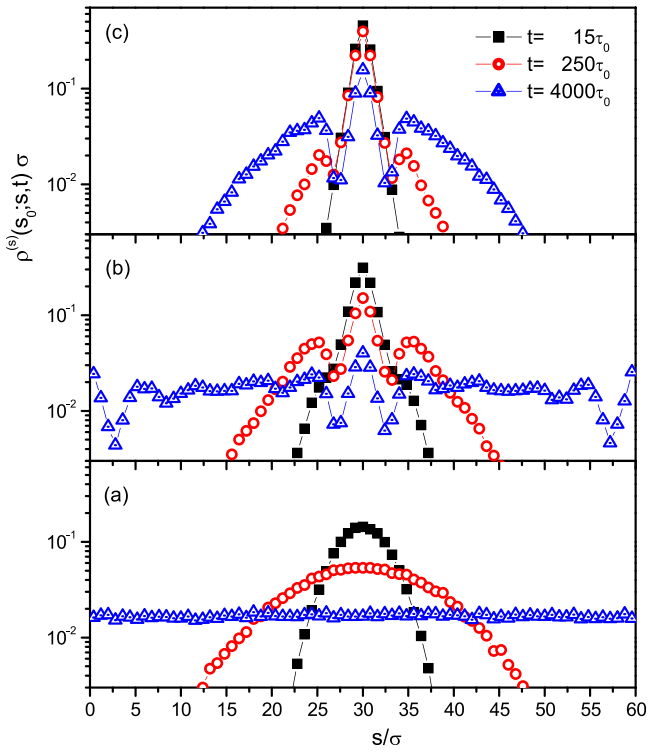

FIG. 4. The dimensionless self-distribution functions $\rho^{(s)}(s_0; s, t)\,\sigma$ for $N = 10$, $\Gamma = 125$, and the initial position $s_0 = 30.00\,\sigma$ corresponding to the eccentricities: $\varepsilon = 0.00$ in panel (a), $\varepsilon = 0.98$ in panel (b), and $\varepsilon = 0.99$ in panel (c).

$t = 250\,\tau_0$ the plot for this function still has the Gaussian bell-like shape also characteristic of the system with uniform curvature. This exemplifies why the width of the bell, or mean-square angular displacement, is sufficient to describe the diffusion of particles along a circle.

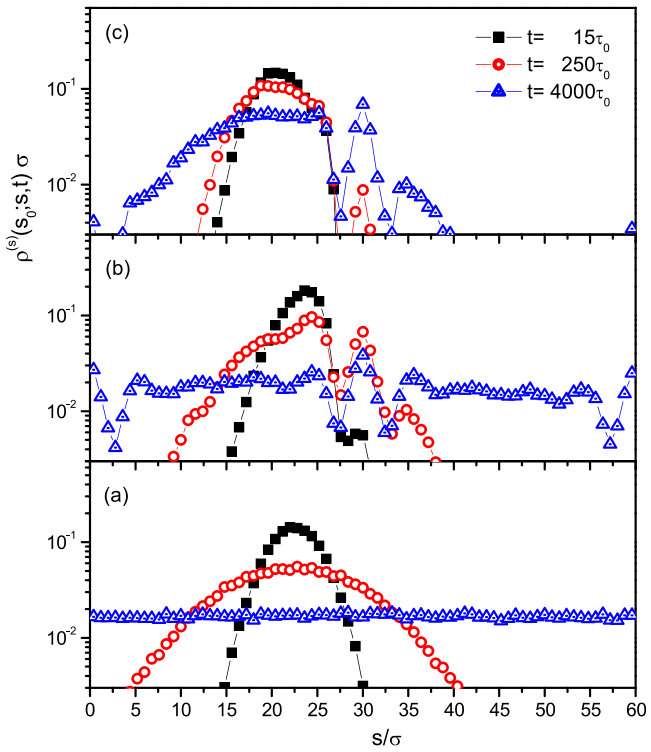

FIG. 5. The dimensionless self-distribution functions $\rho^{(s)}(s_0; s, t)\,\sigma$ for $N = 10$, $\Gamma = 125$, and the initial position $s_0 = 22.50\,\sigma$ corresponding to the eccentricities: $\varepsilon = 0.00$ in panel (a), $\varepsilon = 0.98$ in panel (b), and $\varepsilon = 0.99$ in panel (c).

The effects induced by a gradient in the curvature are then illustrated in the middle and upper panels of these figures. For the situation reported in Figure 4, the tagged particle starts exactly at the left vertex, where the curvature is largest, and diffuses evenly to the right and left of this point, like in the situation with uniform curvature, yet the bell-like shape is rapidly lost when $\varepsilon \neq 0$. The peak in the initial position indeed decreases, but now two off-center peaks have simultaneously developed for $t = 250\,\tau_0$, with the in-between valleys showing again the preference for a particle to stay at this vertex. In the instance of $\varepsilon = 0.98$, the self-diffusion distribution almost reaches its asymptotic form at $t = 4000\,\tau_0$, as can be confirmed, according to Equation (13), by comparing with the related (properly normalized) plot shown in panel (b) of Figure 1, whereas for $\varepsilon = 0.99$ at the same point in time it seems to be rather away from this limit. Hence, there is a noticeable dynamic transition when the particles in the upper half of the loop start to interact with those in the lower half, which brings about a drastic slowing down of the tagged particle self-diffusion.

These trends are also evident in the situation presented in Figure 5, where the tagged particle begins at the middle point between the top and left vertices. Here, the sharp peak located at $s_0 = 30.00\,\sigma$ that becomes apparent for $t = 250\,\tau_0$, in both cases with $\varepsilon \neq 0$, shows once more the trapping of particles in the positions with highest local curvature; furthermore, the onset of the restrained regime is now apparent in the lack of symmetry for the case with $\varepsilon = 0.99$ when $t = 4000\,\tau_0$. The self-distribution function for the case with $\varepsilon = 0.98$, on the other hand, is once more close to reaching its asymptotic form at the latest reported time.

The reduction in the mobility of the particles ensuing from the interference between the top and bottom halves of the most stretched system is naturally reduced when the interaction among the particles decreases. This is illustrated in Figure 6, which presents the results for $\rho^{(s)}(s_0; s, t)$ corresponding to $N = 10$, $\varepsilon = 0.99$, and $\Gamma = 64$ (in which case the effective diameter is approximately $4.0\,\sigma$). Three initial positions for the tagged particle are portrayed: $s_0 = 22.50\,\sigma$ in panel (a), $s_0 = 26.25\,\sigma$ in panel (b), and $s_0 = 30.00\,\sigma$ in panel (c). Now, even for the very elongated system the self-distribution function almost gets to its asymptotic shape at $t = 4000\,\tau_0$, as can be checked out by comparing the corresponding results in the three panels—which are not yet completely identical, but are nonetheless pretty close to each other.

In the top panel of Figure 6, which is akin to the top panel of Figure 4, the tagged particle again diffuses symmetrically in both directions, but for $\Gamma = 64$, the distribution profile spreads more swiftly, and at the latest reported time it reaches a roughly even distribution over the whole loop, save for the peaks at the vertices of highest curvature. When the tagged particle starts at the middle point between the top and left vertices, as shown in the bottom panel of Figure 6 and the top panel of Figure 5, the plot of $\rho^{(s)}(s_0; s, t)$ rapidly evolves into a skewed-bell contour with the emergence (for example, when $t = 250\,\tau_0$) of a distinct peak located at $s_0 = 30.00\,\sigma$, framed by sharp valleys that indicate the appearance of kinetic

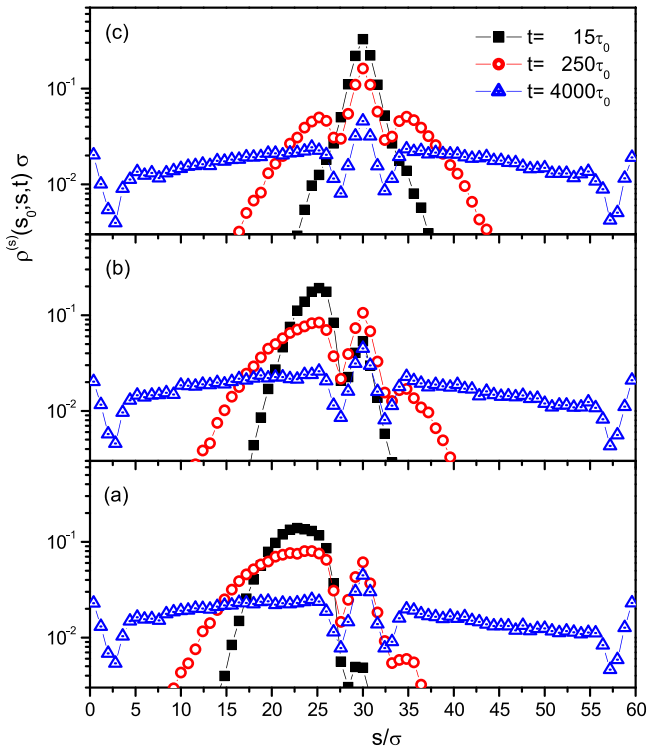

FIG. 6. The dimensionless self-distribution functions $\rho^{(s)}(s_0; s, t)\,\sigma$ for $N = 10$, $\Gamma = 64$, and $\varepsilon = 0.99$ corresponding to the initial positions: $s_0 = 22.50\,\sigma$ in panel (a), $s_0 = 26.25\,\sigma$ in panel (b), and $s_0 = 30.00\,\sigma$ in panel (c).

barriers caused by the pinning down of a particle at this vertex.

The evolution of the self-distribution function is then regulated by the leaking of particles through those barriers, and this seeping is indeed hindered as the particle-particle repulsion increases: at $t = 4000\,\tau_0$, we get once more a rather uniform distribution for $\Gamma = 64$, except for peaks at the extremes, although the self-distribution function is still somewhat higher on the upper half than on the lower half of the loop; for $\Gamma = 125$, on the other hand, this function still has someway to go to reach its final shape. The central panel in Figure 6 shows that the proximity of the tagged particle to the vertex of maximum curvature helps to accelerate the leaking process discussed here.

V. CONCLUDING REMARKS

It has been shown here that a nonuniform local curvature plays a determining role in the equilibrium structure and dynamic properties of one-dimensional systems of repulsive colloidal particles. In particular, our systems tend to trap particles within the regions of greatest curvature, an outcome that seems akin to the lightning rod effect. This could be taken as an indicator of analogous behavior for inclusions embedded in membranes, at least when the interaction between such particles is repulsive. Beyond this one-body result, the two-body correlations also exhibit a strong influence from the curvature gradient, with particular stress in the appearance of long-ranged and asymmetric effects. With regard to the self-diffusion process, the anisotropy of the particle movements couples with the position dependence of the net forces acting on each colloid to generate a richer array of phenomena than in the cases with uniform curvature.

No eccentricities in between 0 and 0.98 are reported in Section IV since the corresponding results look very similar to the ones with $\varepsilon \approx 0$; values of a/b larger than 5 are necessary for the effects of the curvature gradients to become evident when $\Gamma = 125$. Additionally, we only report ensemble averages: over 6400 replicas for $g_w(x)$ and $g(s_0, s)$, and over 51 200 for $\rho^{(s)}(s_0; s, t)$. The experimental realization of these calculations may be rather difficult at the moment not only because of the enormous number of copies involved in the averages but also because of the extremely long times to be considered (current experimental setups are limited to tracking times of at most some 10 h without interruptions[24]).

Nevertheless, only a few isolated reproductions of our systems should be necessary in order to generate, within the error bars, the same results that are shown here for $\Gamma = 125$ with $\varepsilon \leq 0.98$, as well as those for $\varepsilon = 0.99$ with $\Gamma = 64$. For the case of $\varepsilon = 0.99$ with $\Gamma = 125$, however, things may be quite different. From our calculations we can say, for that instance, that in isolated events the particles can get stuck. In such a situation, the concentration profile $g_w(x)$ has the appearance of two coupled gears, one in the upper half of the ellipse and the other in the lower half, trying to move in opposite directions. Single particles are thus confined to very narrow regions and only there can they diffuse.[25] This result yields an interesting observation: it may be possible to arrest, or release, the system simply by increasing, or decreasing, the external magnetic field. Similar results may be achieved by varying the eccentricity, though this seems to be somewhat more complicated.

ACKNOWLEDGMENTS

Financial support by Conacyt (Grant No. 237425 and Red Temática de la Materia Condensada Blanda) is gratefully acknowledged. The authors also thank the General Coordination of Information and Communications Technologies (CGSTIC) at Cinvestav for providing HPC resources on the Hybrid Cluster Supercomputer "Xiuhcoatl," which have contributed to the research results reported in this paper.

[1] M. Weiss, H. Hashimoto, and T. Nilsson, Biophys. J. **84**, 4043 (2003).
[2] V. M. Sukhorukov and J. Bereiter-Hahn, PLoS One **4**, e4604 (2009).
[3] N. Malchus and M. Weiss, Biophys. J. **99**, 1321 (2010).
[4] Q.-H. Wei, C. Bechinger, and P. Leiderer, Science **287**, 625 (2000).
[5] F. Zhang, G. G. Long, P. R. Jemian, and J. Ilavsky, Langmuir **24**, 6504 (2008).
[6] S. Savarala, S. Ahmed, M. A. Ilies, and S. L. Wunder, ACS Nano **5**, 2619 (2011).
[7] P. Castro Villarreal, A. Villada Balbuena, J. M. Méndez Alcaraz, R. Castañeda Priego, and S. Estrada Jiménez, J. Chem. Phys. **140**, 214115 (2014).
[8] D. L. Ermak and J. A. McCammon, J. Chem. Phys. **69**, 1352 (1978).
[9] P. C. Villarreal, J. Stat. Mech.: Theory Exp. **2010**, P08006.
[10] P. C. Villarreal, J. Stat. Mech.: Theory Exp. **2014**, P05017.
[11] E. Curotto and M. Mella, J. Chem. Phys. **142**, 114111 (2015).
[12] F. Manca, P.-M. Déjardin, and S. Giordano, Ann. Phys. **528**, 381 (2016).
[13] A. Taloni, O. Flomenbom, R. Castañeda Priego, and F. Marchesoni, Soft Matter **13**, 1096 (2017).
[14] A. Villada Balbuena, M.S. thesis, Cinvestav, Mexico, 2013.
[15] M. Kollmann, Phys. Rev. Lett. **90**, 180602 (2003).

[16]C. Lutz, M. Kollmann, and C. Bechinger, Phys. Rev. Lett. **93**, 026001 (2004).
[17]P. X. Viveros Méndez, J. M. Méndez Alcaraz, and P. González Mozuelos, J. Chem. Phys. **136**, 164902 (2012).
[18]K. Zahn, J. M. Méndez Alcaraz, and G. Maret, Phys. Rev. Lett. **79**, 175 (1997).
[19]P. X. Viveros Méndez, personal communication (2016).
[20]X.-G. Ma, P.-Y. Lai, and P. Tong, Soft Matter **9**, 8826 (2013).
[21]G. Nägele, Phys. Rep. **271**, 215 (1996).
[22]J. P. Hansen and I. R. McDonald, *Theory of Simple Liquids* (Elsevier, 2006).
[23]P. X. Viveros Méndez, J. M. Méndez Alcaraz, and P. González Mozuelos, J. Chem. Phys. **128**, 014701 (2008).
[24]M. A. Escobedo Sáchez and C. Zunke, personal communication (2017), We refer here to typical video-microscopy setups on two-dimensional or quasi-two-dimensional colloidal systems, which are subject to thermal (convection, evaporation), mechanical (the sample cell is not completely flat but most of the time slightly titled), and biological (sooner or later the systems become infected with some bacteria from the laboratory environment) instabilities, as well as to variations in the computer, video-camera, lamps, etc. All these effects together cause that monitoring of the particles must be interrupted at some point; a conservative maximum would be about 10 h. This does not mean however that the situation cannot be improved over time.
[25]O. A. Ramírez Garza, M. S. thesis, Cinvestav, Mexico, 2015.